Counting fluorescently labeled proteins in tissues in the spinning–disk microscope using single–molecule calibrations

Maijia Liao†, Yin–Wei Kuo†, and Jonathon Howard*
Department of Molecular Biophysics and Biochemistry, Yale University, New Haven, CT 06520

ABSTRACT **Quantification of molecular numbers and concentrations in living cells is critical for testing models of complex biological phenomena. Counting molecules in cells requires estimation of the fluorescence intensity of single molecules, which is generally limited to imaging near cell surfaces, in isolated cells, or where motions are diffusive. To circumvent this difficulty, we have devised a calibration technique for spinning–disk confocal microscopy, commonly used for imaging in tissues, that uses single–step bleaching kinetics to estimate the single–fluorophore intensity. To cross–check our calibrations, we compared the brightness of fluorophores in the SDC microscope to those in the total internal reflection and epifluorescence microscopes. We applied this calibration method to quantify the number of end–binding protein 1 (EB1)–eGFP in the comets of growing microtubule ends and to measure the cytoplasmic concentration of EB1–eGFP in sensory neurons in fly larvae. These measurements allowed us to estimate the dissociation constant of EB1–eGFP from the microtubules as well as the GTP–tubulin cap size. Our results show the unexplored potential of single–molecule imaging using spinning–disk confocal microscopy and provide a straightforward method to count the absolute number of fluorophores in tissues that can be applied to a wide range of biological systems and imaging techniques.**

Monitoring Editor
Jennifer Lippincott–Schwartz
Howard Hughes Medical Institute

Received: Dec 17, 2021
Revised: Mar 17, 2022
Accepted: Mar 18, 2022

INTRODUCTION

Measuring the concentration and stoichiometry of macromolecules is essential for quantitatively testing models of dynamic biological processes (Howard, 2014; Pollard, 2014). A potentially general method for counting molecules in living cells is to estimate the intensity of single molecules so that concentrations can be deduced from fluorescence images (Coffman and Wu, 2012; Elf and Barkefors, 2019). This approach has been used successfully to study cell signaling (Mashanov *et al.*, 2004; Uyemura *et al.*, 2005; Ulbrich and Isacoff, 2007), cytokinesis (Wu and Pollard, 2005), mitosis (Joglekar *et al.*, 2006), transcription (Elf *et al.*, 2007; Taniguchi *et al.*, 2010; Tutucci *et al.*, 2018), bacterial motility (Leake *et al.*, 2006), and development (Gross *et al.*, 2019).

The absolute quantification of single–molecule fluorescence is challenging, however, especially in tissues. Several quantification approaches have been taken, but all have drawbacks. For example, the intensity of fluorescently labeled molecules (such as GFP–tagged proteins) can be calibrated by quantitative immunoblotting (Rusan *et al.*, 2001; Wu and Pollard, 2005; Seetapun *et al.*, 2012). While this strategy is suitable for cultured cell lines or unicellular organisms, it cannot be applied to tissues due to the difficulty of isolating single cell types for immunoanalysis. A second approach is to visualize single fluorophores and to use single–step bleaching to estimate the single–molecule fluorescence (Leake *et al.*, 2006; Engel *et al.*, 2009; Coffman *et al.*, 2011). A limitation is that it generally requires a combination of strong illumination and low fluorophore density, for example total internal reflection fluorescence (TIRF) imaging near the cell surface (Leake *et al.*, 2006; Ulbrich and Isacoff, 2007), and is therefore not suitable for imaging deep in tissues or structures containing a larger number of fluorophores. A third

This article was published online ahead of print in MBoC in Press (http://www.molbiolcell.org/cgi/doi/10.1091/mbc.E21–12–0618) on March 24, 2022.

†These authors contributed equally to this work.

Author contributions: M.L. and Y.–W.K. performed all experiments and data analysis; all authors designed the research and wrote the paper.

*Address correspondence to: Jonathon Howard (joe.howard@yale.edu).

Abbreviations used: ADU, analogue–to–digital unit; da, dendritic arborization; EB1, end–binding protein 1; MC, Monte Carlo; MT, microtubule; SDC, spinning–disk confocal; TIRF, total internal reflection fluorescence.

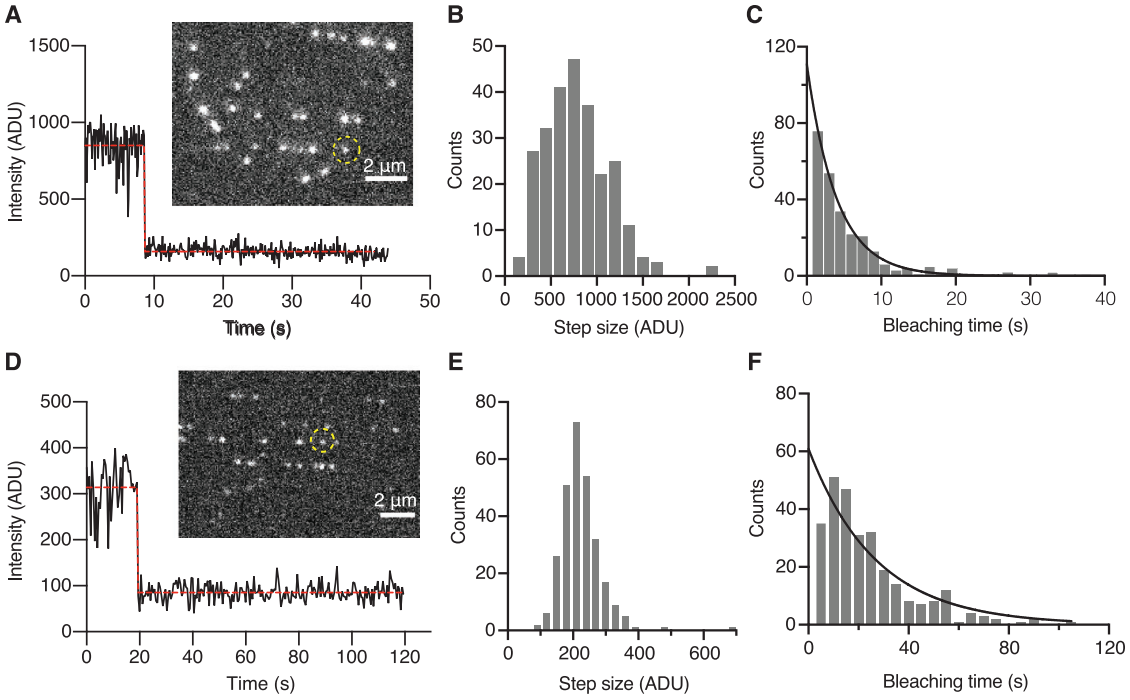

FIGURE 1: Visualization of single–Alexa Fluor 488 fluorophores by TIRF and SDC microscopies. (A) The black trace shows the intensity as a function of time of a single punctum imaged by TIRF (circled in the inset image). The red dashed line corresponds to a single step identified by the algorithm described in *Materials and Methods*. Single–step bleaching can be clearly observed. (B) Histogram of step sizes. (C) Histogram of bleaching times. (D) The black trace shows the intensity as a function of time of single puncta imaged using a Nikon SDC microscope with Yokogawa disk (circled in the inset image). The red dashed line corresponds to a single step. Single–step bleaching can be clearly observed. (E) Histogram of step sizes. (F) Histogram of bleaching times. The sample irradiance was 320 and 290 kW/m^2 in TIRF and SDC, respectively. The images were acquired with 100 and 500 ms exposure times in TIRF and SDC, respectively. ADU: analogue–to–digital unit.

approach is fluorescence correlation spectroscopy (FCS) (Magde *et al.*, 1972; Wachsmuth *et al.*, 2015) or number and brightness (N&B) (Cutrale *et al.*, 2019), which uses the fluctuations of the fluorescence intensity of the fluorophore–tagged biomolecules in a small volume to obtain quantitative information such as their abundance and mobility. However, these methods are designed for diffusing molecules and are not suitable for molecules undergoing directed motion. Thus, these techniques are either difficult to apply in tissues directly or restricted to the quantification of biomolecules that are dilute or diffusing.

In this work we visualized single fluorophores in a spinning–disk confocal (SDC) microscope, a commonly used instrument for live–cell imaging in tissues, and used single–step photobleaching to calibrate fluorescence intensity. While visualization of single fluorophores has been achieved routinely using TIRF, laser–scanning confocal, and epifluorescence microscopies, single–fluorophore intensities in the SDC microscope reported in earlier studies have been too low to use as calibration standards (Lawrimore *et al.*, 2011). Here, we compared the fluorescence intensities and photobleaching kinetics in a commercial SDC microscope to those in TIRF and epifluorescence microscopes, to identify the theoretical and practical limitations on the sensitivity of the SDC microscope. The single–fluorophore intensity measured by SDC microscopy serves as a direct calibration standard for fluorophore counting. As a proof of principle, we quantified the number of end–binding protein 1 (EB1)–eGFP in the EB1 comets and the concentration of free EB1–eGFP in the dendrites of *Drosophila* class IV dendritic arborization (da) sensory neurons. Our results provide an estimation of the GTP–cap size and the binding affinity of EB1–eGFP, crucial information for characterizing the dynamic and biochemical properties of neuronal microtubules (MTs).

RESULTS AND DISCUSSION

Single fluorophores can be observed by SDC microscopy

To quantify molecular fluorescence in a commercial SDC microscope (Nikon Ti Elipse, Yokagawa spinning disk, 50 µm pinhole, 100 mW diode lasers), we measured the intensities of single fluorophores. Stabilized MTs labeled with a low density of Alexa Fluor 488 were affixed to the surface of the coverslip by anti–tubulin antibodies. We first calibrated molecular fluorescence by TIRF microscopy (Figure 1A, inset), a common method for single–molecule imaging. The intensities of the fluorescent puncta usually decreased in a single step (Figure 1A), showing that the majority of puncta corresponded to single–Alexa Fluor 488 dye molecules, as expected. The average intensity of single Alexa Fluor 488 was measured from the histogram of step sizes (Figure 1B), and the bleaching rate was determined by fitting the bleaching time histogram to an exponential (Figure 1C). Next, we imaged the MTs by SDC microscopy. We observed fluorescent puncta that resembled the single fluorophores seen by TIRF (Figure 1D, inset). The intensity traces of individual puncta showed clear single–step bleaching events, confirming that the fluorescence signals originated from single fluorophores (Figure 1D). The fluorophore intensity and bleaching rate were measured from the step–size and bleaching time histograms, respectively (Figure 1, E and F). These results demonstrated that single–molecule imaging by SDC microscopy is possible.

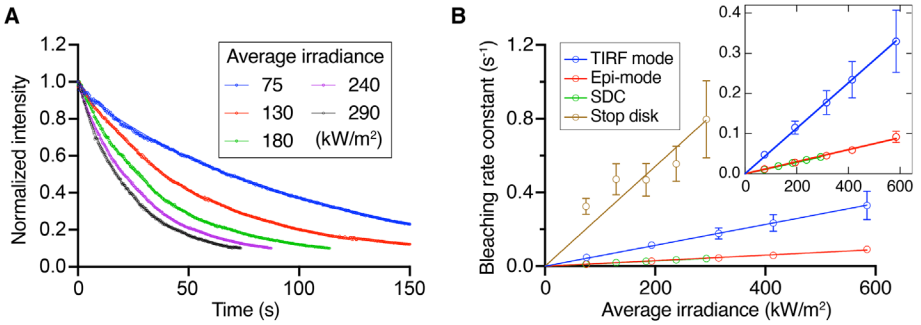

FIGURE 2: Bleaching rate measurements in different imaging methods. (A) Example bleaching curves under different illumination irradiances in the SDC microscope. The initial segment of each bleaching curve (until ~10% of initial intensity) was fitted to a single–exponential decay (solid lines). (B) Bleaching rate constants derived from the exponential fits increased linearly with irradiance. Inset: zoom–in of the bottom three lines. Solid lines: linear regressions constrained to pass through the origin. Error bars: SD from three experimental measurements in each condition.

Comparison of excitation intensities in the SDC, TIRF, and epifluorescence microscopes

The fluorescence intensities of single fluorophores were dimmer in the SDC microscope compared with the TIRF microscope even when the camera exposure time was five times longer (under similar excitation laser power; Figure 1, B and E). This is due to differences in excitation intensities and emission detection efficiencies. To investigate the excitation intensity differences, we imaged MTs labeled with a high density of Alexa Fluor 488 in the TIRF, epifluorescence, and SDC microscopes. We estimated the intensities of the local excitation fields by measuring the fluorescence bleaching under the same illumination irradiances (the laser power out of the objective divided by the illuminated area). The decay of the fluorescence intensities was well described by single exponentials (see examples in Figure 2A), and the bleaching rates (obtained from the exponential fit) increased linearly with average illumination irradiance (Figure 2B), as expected because we are well below the fluorescence saturation intensity (see below).

Under the same illumination irradiances, the bleaching rate constant was 3.8 ± 0.2 (mean ± SE unless otherwise noted) times larger in TIRF compared with epifluorescence microscopy (measured from the slopes of the linear regression; Figure 2B and Table 1). The roughly four–times–higher bleaching rate in TIRF over epifluorescence accords with the approximately fourfold enhancement of the evanescence field intensity predicted theoretically (derived in the Supplemental Information, and see Martin–Fernandez *et al.*, 2013). This is the first quantification of enhancement of the evanescence field intensity that we are aware of.

The bleaching rate constants measured from the highly labeled MTs (TIRF: 5.7 ± 1.0 s; SDC: 24.0 ± 1.1 s; Table 2; details in *Materials and Methods*) were in good agreement with the bleaching rate constants obtained from the single–molecule bleaching times (TIRF: 5.3 ± 1.1 s; SDC: 24 ± 3 s). This is further confirmation of the reliability of our single–molecule SDC observations.

Under the same illumination irradiances, the bleaching rate constants of SDC and epifluorescence were similar (ratio of slopes = 0.96 ± 0.04) (Figure 2B and Table 1). This shows that the excitation field intensities are similar in the two imaging modes when the irradiance is the same, as expected.

In SDC, each point in the sample is illuminated intermittently due to the rotation of the spinning disk; therefore, only a small percentage of the total area is illuminated at any one time. To assess the effect of the disk rotation, we measured the bleaching rate in illuminated regions when the disk was stationary (i.e., the stop–disk condition). When the disk was stationary, the bleaching rate was 19 ± 1 times larger than in the spinning–disk mode (Figure 2B and Table 1). The instantaneous irradiance of each spot was thus about 20 times larger than the average irradiance, and only ~5% of the field of view was illuminated by the excitation light when the disk was spinning. This result confirms that most of the illumination light is blocked by the spinning disk, transmitting only a small portion of excitation light at each point of the sample.

In summary, the higher fluorescence intensities in the TIRF microscope are due in part to the fourfold enhancement of the intensity of the evanescence field that excites the fluorophores. The excitation intensities in epifluorescence and SDC are similar when the instantaneous illumination in the SDC is increased roughly 20–fold to compensate for the attenuation due to the small fraction of the spinning disk occupied by the pinholes.

Comparison of emission efficiencies in the SDC, TIRF, and epifluorescence microscopes

We next compared the fluorescence intensities of the highly labeled Alexa Fluor 488 MTs when imaged by the TIRF, epifluorescence, and SDC microscopes. Consistent with the single–molecule measurements, fluorescent MTs were the brightest by TIRF microscopy and dimmest by SDC microscopy (Figure 3A) under similar illumination irradiances and identical camera exposure times. Like the bleaching rates, the fluorescence intensities increased linearly with increasing illumination irradiance (Figure 3B), showing that the excitation light intensity is within the linear dynamic range. This is expected because the excitation intensity we used was much smaller than the predicted saturation intensity of Alexa Fluor 488 (4 GW/m^2, about 10,000 times higher than the maximum irradiance we used). From the slopes of the linear regression, TIRF microscopy is 3.5 ± 0.2 times brighter than epifluorescence (Table 3), which agrees well with the 3.8 ± 0.2–fold increase in TIRF's excitation field measured from the bleaching rate (Table 1) and is expected from the enhancement of the evanescence field intensity in TIRF (mentioned above). However, the SDC fluorescence intensity was 3.6 ± 0.1–fold lower than that of epifluorescence (Figure 3B and Table 3), even though the excitation intensities were similar (as judged by the similar bleaching rates stated above). The lower intensities of the SDC images compared with those of epifluorescence indicate that the SDC microscope suffers more light loss in the emission pathway. The loss is not due to the objective as the same objective was used. Some of the

Fit value ± SE	TIRF	Epifluorescence	Spinning disk	Stop disk
Slope ($10^3 \cdot s^{-1} \cdot W^{-1} \cdot m^2$)	570 ± 30	150 ± 5	144 ± 2	2700 ± 200

TABLE 1: Slopes of bleaching rate constant versus irradiance.

Mean ± SD[a]	TIRF, single fluorophore	TIRF, high fluorophore density MT	SDC, single fluorophore	SDC, high fluorophore density MT	Tetraspeck bead (TIRF)	Tetraspeck bead (SDC)
Bleaching time (s)	5.3 ± 1.1	5.7 ± 1.0	24 ± 3	24.0 ± 1.1	n/a	n/a
Step size per 100 ms exposure time (ADU)	600 ± 160	—	47 ± 3	—	—	—
Intensity per µm of MT ADU for 100 ms exposure time	—	6.1 ± 1.0 × 10^5	—	4.4 ± 0.2 × 10^4	—	—
Total intensity per bead per 100 ms exposure time (ADU)	—	—	—	—	1.34 ± 0.23 × 10^5	1.06 ± 0.04 × 10^4
Average irradiance (W/cm^2)	32	32	29	29	32	29
Estimated fluorophore labeling density[b]	59%	54%	n/a			

[a]SD from $n = 3$ measurements.
[b]Fluorophore density estimated by absorbance is 43 ± 1% ($n = 3$ measurements).

TABLE 2: Single–fluorophore fluorescence intensity and bleaching time in TIRF and SDC microscopy.

Fit value ± SE	TIRF	Epifluorescence	Spinning disk
Slope ([ADU/µm]·W^{-1}·m^2)	1.91 ± 0.07	0.54 ± 0.01	0.152 ± 0.003

TABLE 3: Slopes of fluorescence intensity per micron of MT versus irradiance.

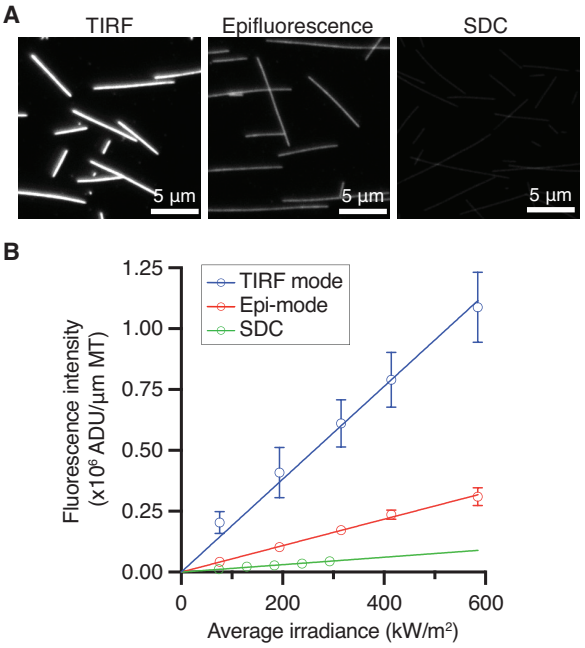

FIGURE 3: Fluorescence intensities of Alexa Fluor 488 MTs. (A) Example images of Alexa Fluor 488 MTs imaged by TIRF, epifluorescence, and SDC microscopy under similar average illumination irradiances (76 kW/m^2 for TIRF and epifluorescence; 75 kW/m^2 for SDC) with the same camera exposure time (100 ms). Images were adjusted to the same contrast level. (B) Fluorescence intensities increased linearly with average irradiance in all three imaging methods. Error bars: SD. Each condition was measured from three experimental measurements. Solid lines: linear regression of each imaging method. The linear regression is constrained at the origin.

loss is expected to be due to the pinhole (~20%; Supplemental Figure S1; Wilson, 1990); the rest of the loss is presumably due to the lenses, mirrors, and filters. In summary, we have accounted for the lower fluorescence intensity measured in SDC microscopy compared with that in wide–field (epifluorescence and TIRF) microscopy as a combination of different excitation intensities and emission efficiencies.

As an overall check on our single–molecule fluorescence calibrations, we estimated the density of the Alexa Fluor 488 in the highly labeled MTs. The density was 59% (estimated by TIRF) and 54% (estimated by SDC); these values are similar to the labeling density estimated by absorbance using a spectrophotometer (43 ± 1%; mean ± SD) (Table 2). Therefore, we have established a calibration standard for fluorophore counting by measuring the bleaching step size of single fluorophores using SDC microscopy.

Establishing a consistent calibration standard for fluorophore counting with SDC microscopy

To facilitate calibration of the single–molecule fluorescence in the SDC microscope, we used fluorescent beads as a reference standard. We imaged TetraSpeck beads (Thermo Fisher, cat no. T7279) in both the TIRF and SDC microscopes under the same imaging conditions as for the single–fluorophore experiments. The intensity ratios of TetraSpeck beads to single–Alexa Fluor 488 dyes measured by TIRF and SDC were 225 ± 72 (mean ± SE) and 227 ± 18, respectively (Table 2). By periodically measuring the intensity of TetraSpeck, we could test whether there has been a change in the excitation or emission intensities of the SDC microscope.

When using different fluorophores, we adjusted the calibration based on the relative brightness compared with Alexa Fluor 488 at the illumination wavelengths, as well as considering the sample irradiance (laser intensity setting) and the camera exposure time.

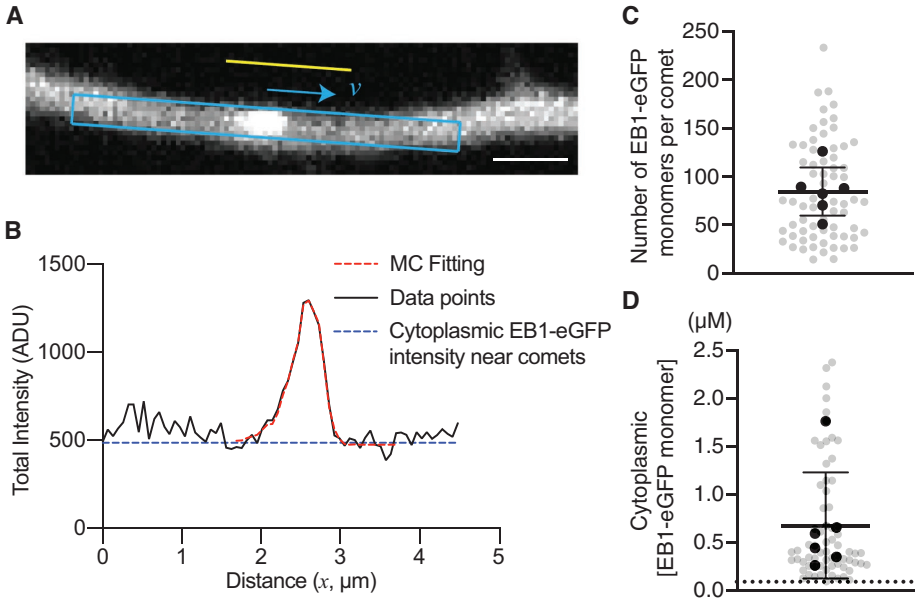

FIGURE 4: Determination of the amount of EB1–eGFP at MT ends and cytoplasm. (A) An example of an EB1–eGFP comet. The overall intensity was calculated within the 0.5 μm × 4.5 μm blue rectangle. The intensity of adjacent regions outside of the dendrite (yellow line) was used for background subtraction (see discussion in Supplemental Figure S2). Scale bar 1 μm. (B) The measured intensity profile (black) was modeled as an exponential convolved with a Gaussian point–spread function (red dashed line; see *Materials and Methods*). The offset (blue line) is considered to be the cytoplasmic EB1–eGFP intensity. (C) Number of EB1–eGFPs per comet. (D) Concentration of cytoplasmic EB1–eGFP. Black points indicate the average from each larva (six larvae; data points from all 68 comets are shown in light gray). The minimum concentration that can be detected (signal–to–noise ratio > 3) was ~0.09 μM (dashed line in D). Mean and SD from six larvae are shown as horizontal bars.

Drosophila larvae under cell–specific promoters (Rolls *et al.*, 2007; Han *et al.*, 2011). EB1 preferentially binds to growing MT ends and turns over rapidly; in this way it forms a comet–like distribution behind the polymerizing tip of the MT (Bieling *et al.*, 2007; Dixit *et al.*, 2009). Imaged by SDC microscopy, fluorescent comets were observed throughout the dendrites of these neurons (example in Figure 4A). To measure the shapes of the comets, we modeled the comets as exponential decays convolved with a Gaussian point–spread function using a Monte Carlo (MC) optimization procedure (red dashed curve in Figure 4B and see Supplemental Figures S3–S5 and *Materials and Methods* for details). By considering the fluorophore brightness (i.e., the product of extinction coefficient and quantum yield), emission spectra, illumination irradiance, and camera exposure time, we determined the intensity of a single eGFP using the bleaching step size of Alexa Fluor 488 as a calibration standard (see *Materials and Methods* for details). We found that each comet contains on average 84 ± 25 (mean ± SD, n = 6 larvae) EB1–eGFP monomers (Figure 4C), with an exponential decay length λ of 190 ± 40 nm. If we assume that EB1 binds to GTP–tubulin in the lattice, then the GTP–cap has an average length of 190 nm (where the density decreases e–fold). Given that there are 300 tubulin dimers in 190 nm (assuming the dimer length is 8.2 nm and there are 13 protofilaments and that the GTP–tubulin density decays exponentially from 100% at the end) and EB1 has been suggested to exist as a dimer (Seetapun *et al.*, 2012; Sen *et al.*, 2013), we estimate that 14% of the GTP–tubulins have EB1–eGFP dimer bound (occupancy η = 42/300, assuming one EB1 dimer binds to one GTP–tubulin subunit and EB1–eGFP is much more abundant than the unlabeled EB1).

The accuracy of our calibration is primarily determined by the accuracy of the step size measured in the SDC, which had a coefficient of variance of 0.07 (SD/mean in three independent measurements). From the t distribution, the 95% confidence interval is $\pm 0.07 \times 2.92 \cong 0.2$ (2 degrees of freedom). Other sources of error include measurement of the irradiance (<5% SD/mean) and uncertainties of the fluorescence intensities inside the cell due to molecular interactions. The latter effects are difficult to judge. Overall, we expect our calibration to be accurate around 20% (SD/mean), which makes the 95% confidence range roughly a factor of two (between 0.6 and 1.4).

Quantification of EB1–eGFP in *Drosophila* neurons

MT EBs track growing MT ends in vitro and in vivo. The amount and the size of the EB binding zone on a growing MT tip can serve as an indicator of the GTP–tubulin cap size (Zanic *et al.*, 2009; Maurer *et al.*, 2011; Seetapun *et al.*, 2012; Coombes *et al.*, 2013; Strothman *et al.*, 2019; Roostalu *et al.*, 2020). Additionally, EBs can recruit various MT–associated proteins that may be critical for the dynamics and function of MT filaments (Akhmanova and Steinmetz, 2015). While the number and direction of EB comets are frequently used to estimate the number and polarity of growing MTs in neurons (Stone *et al.*, 2008; Stewart *et al.*, 2012; del Castillo *et al.*, 2015), the absolute number and binding region of EB molecules have not been examined in detail. Quantifying the amount of EB proteins at a growing MT end, the size of the EB–binding region (i.e., the EB–cap size), and its binding affinity thus provide valuable insights into the dynamical properties of the MT cytoskeleton.

To quantify EB comets in vivo, we expressed EB1–eGFP and the cell membrane marker CD4–tdTomato in class IV neurons of

The cytoplasmic EB1–eGFP monomer concentration was 0.68 ± 0.55 μM (Figure 4D; mean ± SD, n = 6 larvae; see *Materials and Methods* for details), which is within the large range of physiological EB1 concentrations reported from various species and cell types (from ~0.14 μM monomer in budding yeast to 2.1 μM monomer in HeLa cells) (see references in Supplemental Table S1). Combining these measurements, we can estimate the binding affinity between EB1–eGFP dimer and GTP–tubulin lattice by K_D = [EB1 – eGFP monomer]$_{cytoplasm}/2 \times \left(\frac{1}{\eta} - \frac{1}{\alpha}\right)$ (assuming that unlabeled EB1 and EB1–eGFP have the same affinities), where K_D is the dissociation constant, η is the occupancy of EB1–eGFP (the number of EB1–eGFP dimers bound divided by the total GTP–tubulin sites in the lattice), and α is the fraction of EB1 monomers containing eGFP (i.e. the labeling density). If we assume α is equal to 1, $K_D = 1.9 \pm 0.9$ μM (mean ± SD, n = 6 larvae), which is similar to the dissociation constant estimated in human tissue culture cells (3.8 μM; Seetapun *et al.*, 2012), but much larger than the one reported from in vitro measurements (22 nM; Maurer *et al.*, 2014) (Supplemental Table S2). This estimation represents an upper bound of K_D because we assumed that the overexpressed EB1–eGFP is much more abundant

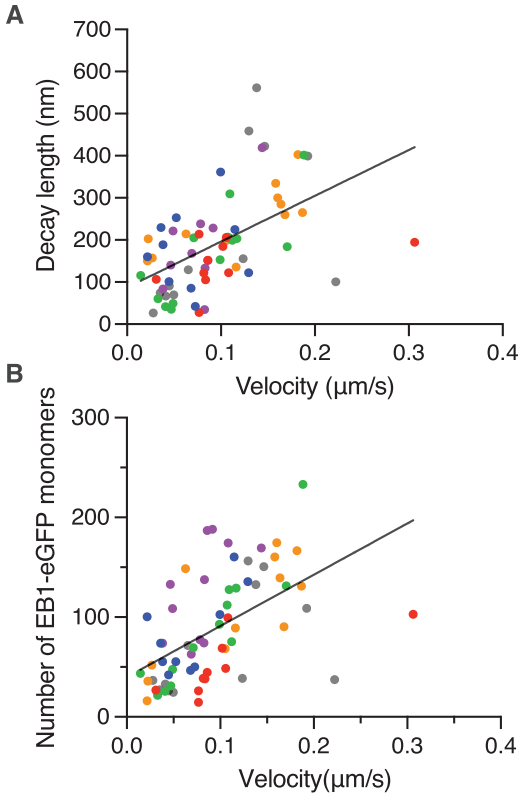

FIGURE 5: Comet velocity positively correlates with the comet decay length. (A) The comet length correlates with velocity. (B) The number of EB1–eGFP dimers correlates with velocity. Pearson correlation coefficients are 0.53 and 0.55, respectively (two–tailed Pearson correlation test, $p < 0.0001$, $n = 68$ comets). Comets from six larvae are shown in different colors.

than the endogenous unlabeled EB1. Thus, our results suggest that these neurons expressed a few hundred nM of EB1–eGFP, with micromolar–level binding affinity to the GTP–tubulin lattice in dendrites.

Previous in vitro studies have shown that the decay length of EB comets increases with the MT polymerization rate (Bieling *et al.*, 2007; Strothman *et al.*, 2019; Farmer *et al.*, 2021). To investigate whether this correlation holds for dendritic MTs, we examined the relationship between the number of EB1–eGFP, the decay length of EB1–eGFP comet, and the comet speed. The comet velocity (0.094 ± 0.057 μm/s, mean ± SD from 68 comets in six larvae, similar to previously reported EB comets speed in *Drosophila* neurons; Ori–McKenney *et al.*, 2012; Poe *et al.*, 2017) showed positive correlations with both decay length and EB1–eGFP number (Pearson's $r = 0.53$ and 0.55, respectively, $n = 68$ comets), suggesting that faster growing MTs have larger GTP–caps and a larger number of bound EB1–eGFP (Figure 5, A and B). These correlations are consistent with previous measurements in a cultured human cell line (Matov *et al.*, 2010) and in the axons of cultured primary neurons from *Drosophila* (Hahn *et al.*, 2021). Our measurements provide additional information, namely the absolute number and affinity of EB1–eGFP in tissues rather than cultured cells.

The GTP–cap size of the dendritic MTs estimated here (~23 layers of tubulin) was only about half of the GTP–cap size estimated in the cultured human LLCPK1 epithelial cells (~55 layers) (Seetapun *et al.*, 2012), potentially reflecting the slower average speed of the dendritic EB comets (94 nm/s in the dendrites, 157 nm/s in LLCPK1 cells; mean ± SE, see Supplemental Table S2 for a summary). Interestingly, the EB–comet lengths observed in the dendrites of *Drosophila* neurons (188 ± 14 nm with a polymerization rate of 94 ± 7 nm/s; mean ± SE) were considerably smaller than the comet lengths of reconstituted MTs with similar growth rates polymerized from purified mammalian brain tubulin (Maurer *et al.*, 2014; Chaaban *et al.*, 2018; Strothman *et al.*, 2019) (summarized in Supplemental Table S2). Instead, the comet length is comparable to those on MTs polymerized from *Caenorhabditis elegans* tubulin; these MTs displayed higher catastrophe frequency than those from mammalian brain tubulin (Chaaban *et al.*, 2018). While the GTP–cap size may not be the sole factor to determine the catastrophe frequency (Bowne–Anderson *et al.*, 2015; Farmer *et al.*, 2021), the shorter cap size may imply more frequent shrinkage events in these dendritic MTs. Live imaging of single MT filaments in the neuron of a whole organism remains a major challenge, leaving the direct measurement of neuronal MT dynamics difficult. Future investigation of the EB–cap size in mutants of MT polymerases, depolymerases, and MT stabilizers can potentially provide new insights into the relationship between GTP–cap size and MT stability in these neurons.

CONCLUSION

We introduced a strategy to quantify the fluorophore number in tissue using SDC microscopy. We imaged single fluorophores in the SDC microscope and used the single–fluorophore bleaching step size to calibrate fluorophore numbers. Applying this strategy, we quantified the number of EB1–eGFP in both puncta–like structures (i.e., EB1 comets) as well as its cytoplasmic concentration, allowing the estimation of binding affinity in vivo. This approach is built on the assumption that the fluorophore intensities inside the cells are similar to the ones measured in vitro, while the brightness of fluorophores may depend on the environments. More detailed intensity corrections can be performed based on previous reports comparing the photoproperties of several fluorescent proteins from both in vitro and in vivo systems (Chen *et al.*, 2002; Heppert *et al.*, 2016; Botman *et al.*, 2019) or using proteins complexes with known copy numbers as internal standards (Thevathasan *et al.*, 2019) to achieve better accuracy.

A major advantage of the strategy introduced here is that the calibration process does not require additional microscopic or biochemical methods and can be performed directly using the identical microscopy setup as in the in vivo imaging experiments. The calibration procedure can be simplified without the needs of extra imaging standards (e.g., fluorescent beads or purified protein standards used for immunofluorescence), tissue fixation, or the isolation of specific cell types from the tissues. Additionally, our fluorescence intensity and bleaching rate measurements using TIRF, epifluorescence, and SDC microscopy provide a quantitative assessment of the minimal brightness required for visualizing single fluorophores using SDC microscopy, which is an important step toward single–molecule imaging in cellular systems. The quantitative imaging methods introduced here are broadly applicable to quantifying the number of target molecules in live cells within tissues, which are typically more challenging systems for other fluorophore-counting methods.

MATERIALS AND METHODS

Flow chamber and MT preparation

Tubulin was purified from bovine brain as previously described (Castoldi and Popov, 2003). The preparation of imaging chambers and stabilized MTs followed the methods described in Gell *et al.* (2010) and Kuo and Howard (2021). All reagents were purchased from Sigma–Millipore except as otherwise noted. To affix the MTs onto the surface of the silanized coverslips, 25 μg/ml anti–tubulin

antibody (clone SAP.4G5) solution was perfused in the flow chamber with 5 min incubation and washed by BRB80 buffer (80 mM PIPES–KOH, pH 6.9, 1 mM ethylene glycol-bis(β-aminoethyl ether)-*N*,*N*,*N*′,*N*′-tetraacetic acid (EGTA), 1 mM $MgCl_2$). The channel was then passivated by incubation with 1% pluronic F127 solution followed by 2 mg/ml casein solution as previously described (Kuo *et al.*, 2019). Alexa Fluor 488–labeled stabilized MTs were prepared by polymerizing Alexa Fluor 488–conjugated bovine tubulin in the presence of slowly hydrolyzable GTP analogue GMPCPP (Jena Bioscience) as previously described (Gell *et al.*, 2010). For single–fluorophore imaging, Alexa Fluor 488 tubulin was mixed with unlabeled tubulin so that the final labeling density of the fluorophore was around 0.09%. Oxygen scavenger solution (40 mM glucose, 40 µg/ml glucose oxidase, 16 µg/ml catalase, 0.1 mg/ml casein, 1% β–mercaptoethanol in BRB80) was used for all fluorescent MT imaging experiments.

Microscopy setup

TIRF and epifluorescence imaging was performed on an inverted microscope (Nikon Ti Eclipse) with a 488 nm excitation laser and a 525/50 nm emission filter. For SDC imaging, an inverted Nikon TI microscope equipped with a confocal scanner unit (CSU–W1 disk; Yokogawa), which contains a four–band dichroic beamsplitter (Di01–T405/488/568/647; Semrock) and a 525/50 nm emission filter, was used. Both microscopes were operated by Nikon NIS element software. All images were collected by a 100×/1.45 NA oil objective (CFI Plan Apochromat Lambda; Nikon) with sCMOS cameras (Zyla 4.2 plus, Andor).

Fly stocks

We used Gal4 driver line *ppk–Gal4* to drive the expression of UAS–EB1–eGFP (Stock 35512 from the Bloomington *Drosophila* Stock Center) to visualize the growing plus ends of MTs and the reporter line, *ppk–CD4–tdTomato* (Han *et al.*, 2011), to observe the dendrite morphology of class IV dendritic arborization (da) neurons.

Larva sample imaging

Embryos were collected for 2 h on apple juice agar plates with a dollop of yeast paste and aged at 25°C in a moist chamber. The plates containing the first batch of embryos were discarded as the dendritic morphology of the da neurons was less consistent in those animals. Larvae were immobilized individually on agarose pads (thickness 0.3–0.5 mm) sandwiched between a slide and a coverslip. The imaging was done using a spinning–disk microscope: the Yokogawa CSU–W1 disk (pinhole size 50 µm) built on a fully automated Nikon TI inverted microscope with perfect focus system and an sCMOS camera (Zyla 4.2 plus sCMOS) and running Nikon Elements software. The EB1 comets in class IV da neurons were imaged with 80% of maximal power for the 488 nm laser and exposure time 200 ms. The tdTomato labeled membrane was imaged with 40% of the maximal power for the 561 nm laser simultaneously.

Measurements of fluorescence intensity and bleaching kinetics

The pixel intensities within 7 × 7 pixel^2 boxes (450 × 450 nm^2) centered at each tetraspeck bead or single fluorophore were summed to get the overall intensity. The background signal was estimated from regions away from fluorescent spots and further subtracted from the overall intensities.

Fluorescence intensity traces for individual Alexa Fluor 488 dyes were obtained by calculating overall intensities over time. To analyze the single–fluorophore photobleaching data, we used the previously developed step detection algorithm that uses statistical tests based on the two–sample *t* test without assumed equal variance to identify steps (Chen *et al.*, 2014). The detected steps smaller than a quarter of the average single bleaching step size were merged with neighboring steps to avoid unrealistic small steps. Steps that last longer than six frames and with signal–to–noise ratios larger than three were used for step size and single–step bleaching time estimations.

Single–fluorophore intensity estimation

The intensity ratio of single eGFP and Alexa Fluor 488 ($I_{eGFP}/I_{Alexa488}$) on SDC microscopy can be estimated based on the following equation:

$$\frac{I_{eGFP}}{I_{Alexa488}} = r_\varepsilon \times r_\Phi \times \frac{\sum_\lambda T \times F_{eGFP} / \sum_\lambda F_{eGFP}}{\sum_\lambda T \times F_{Alexa488} / \sum_\lambda F_{Alexa488}} \times r_{cam} \times r_{ex}$$

where r_ε indicates the ratio of extinction coefficients at excitation wavelength (488 nm); r_Φ is the ratio of quantum yields; *T* is the overall transmittance of the emission filter and dichroic beamsplitter; *F* is the relative emission intensity of the two fluorophores; r_{cam} and r_{ex} correspond to the ratios of camera exposure time and excitation irradiance between the imaging conditions from the in vivo experiments and in vitro single–molecule calibration in the SDC microscope, respectively. The extinction coefficients and quantum yields were obtained from Thermo Fisher and the Fluorescent Protein Database (FPbase). The emission spectra were obtained from the Chroma Spectral Viewer, and the transmittance profiles of the dichroic mirror and emission filters were based on the specifications from the manufacturers. The conversion factor from the spectral properties of fluorophores in our system = 0.65.

Cytoplasmic EB1–eGFP concentration estimation

In the axial dimension, diffraction limits the resolution to $2n\lambda/NA^2$, with *n* the refractive index of the medium between objective and sample, corresponding to a depth of field of ~800 nm. The thickness of most branches studied in this paper fall within the estimated depth of field. Thus, we used the plateau of the MC fitting of the fluorescence signal (Figure 4B, blue dashed line) from the midplane of the dendrite to calculate the cytoplasmic EB1–eGFP concentration. The cytoplasmic EB1–eGFP monomer concentration can be obtained by dividing the total number of local cytoplasmic EB1–eGFP monomers by the volume of the dendrites approximated by $\frac{\pi}{4}D^2L$ (where D is the full width at half maximum of the dendrite from the membrane marker and *L* corresponds to the length of the dendrite where total intensity was extracted).

MC optimization method

The overall intensity profile of the EB1–eGFP comets within 0.5 × 4–8 µm^2 rectangular box can be fitted by $e^{-\left(y-\frac{\sigma^2/\lambda}{2}\right)/\lambda}\,\mathrm{erfc}\left(-\frac{\left(y-\sigma^2/\lambda\right)}{\sqrt{2}\sigma}\right)$ obtained through convolution of the Gaussian with exponential decay, where σ stands for the SD of the Gaussian and λ is the exponential decay length. The fitted parameters are used to set the range of σ and λ, which are used as inputs foar MC optimizations (code details in Github: https://github.com/Maijia-cpu/Comet-profile). In each step of the MC optimization method, a simulated image is generated based on $I_{sim} = Ae^{-\left(y-\frac{\sigma^2/\lambda}{2}\right)/\lambda}\mathrm{erfc}\left(-\frac{\left(y-\sigma^2/\lambda\right)}{\sqrt{2}\sigma}\right)+N$, where *A* stands for the

image intensity and N stands for image photon shot noise. The MC optimization aims to find the σ and λ that minimize the square of the difference (Liao *et al.*, 2021): $D = \sum_{m=0}^{I} \left(I_{sim}^{m} - I_{exp}^{m}\right)^2 I_{exp}^{m}$, where I_{sim} and I_{exp} stand for one–dimensional intensity profiles for simulated and experimental images separately and m stands for pixel number. Six 1000–step simulations were carried out for σ and λ detection. The obtained σ and λ are averages of results from six simulations. The total intensity of the comet was calculated by summing the total experimentally measured signal within the range of $-\sqrt{2}\,\sigma$ to 2λ, with zero being the center of the comets.

ACKNOWLEDGMENTS

We thank Mohammed Mahamdeh for the discussions on the work and the Howard lab members for the feedback on the manuscript. This work was supported by National Institutes of Health Grants R01 NS118884 and R01 GM139337 (to J.H.).

REFERENCES

Akhmanova A, Steinmetz MO (2015). Control of microtubule organization and dynamics: two ends in the limelight. Nat Rev Mol Cell Biol 16, 711–726.

Bieling P, Laan L, Schek H, Munteanu EL, Sandblad L, Dogterom M, Brunner D, Surrey T (2007). Reconstitution of a microtubule plus–end tracking system in vitro. Nature 450, 1100–1105.

Botman D, de Groot DH, Schmidt P, Goedhart J, Teusink B (2019). In vivo characterisation of fluorescent proteins in budding yeast. Sci Rep 9, 1–14.

Bowne–Anderson H, Hibbel A, Howard J (2015). Regulation of microtubule growth and catastrophe: unifying theory and experiment. Trends Cell Biol 25, 769–779.

Castoldi M, Popov AV (2003). Purification of brain tubulin through two cycles of polymerization–depolymerization in a high–molarity buffer. Protein Expr Purif 32, 83–88.

Chaaban S, Jariwala S, Hsu C–T, Redemann S, Kollman JM, Müller–Reichert T, Sept D, Bui KH, Brouhard GJ (2018). The structure and dynamics of C. elegans tubulin reveals the mechanistic basis of microtubule growth. Dev Cell 47, 191–204.e8.

Chen Y, Deffenbaugh NC, Anderson CT, Hancock WO (2014). Molecular counting by photobleaching in protein complexes with many subunits: best practices and application to the cellulose synthesis complex. Mol Biol Cell 25, 3630–3642.

Chen Y, Müller JD, Ruan Q, Gratton E (2002). Molecular brightness characterization of EGFP in vivo by fluorescence fluctuation spectroscopy. Biophys J 82, 133–144.

Coffman VC, Wu JQ (2012). Counting protein molecules using quantitative fluorescence microscopy. Trends Biochem Sci 37, 499–506.

Coffman VC, Wu P, Parthun MR, Wu JQ (2011). CENP–A exceeds microtubule attachment sites in centromere clusters of both budding and fission yeast. J Cell Biol 195, 563–572.

Coombes CE, Yamamoto A, Kenzie MR, Odde DJ, Gardner MK (2013). Evolving tip structures can explain age–dependent microtubule catastrophe. Curr Biol 23, 1342–1348.

Cutrale F, Rodriguez D, Hortigüela V, Chiu CL, Otterstrom J, Mieruszynski S, Seriola A, Larrañaga E, Raya A, Lakadamyali M, *et al.* (2019). Using enhanced number and brightness to measure protein oligomerization dynamics in live cells. Nat Protoc 14, 616–638.

del Castillo U, Winding M, Lu W, Gelfand VI (2015). Interplay between kinesin–1 and cortical dynein during axonal outgrowth and microtubule organization in Drosophila neurons. eLife 4, e10140.

Dixit R, Barnett B, Lazarus JE, Tokito M, Goldman YE, Holzbaur ELF (2009). Microtubule plus–end tracking by CLIP–170 requires EB1. Proc Natl Acad Sci USA 106, 492–497.

Elf J, Barkefors I (2019). Single–molecule kinetics in living cells. Annu Rev Biochem 88, 635–659.

Elf J, Li GW, Xie XS (2007). Probing transcription factor dynamics at the single–molecule level in a living cell. Science 316, 1191–1194.

Engel BD, Ludington WB, Marshall WF (2009). Intraflagellar transport particle size scales inversely with flagellar length: revisiting the balance–point length control model. J Cell Biol 187, 81–89.

Farmer V, Arpa G, Hall SL, Zanic M (2021). Xmap215 promotes microtubule catastrophe by disrupting the growing microtubule end. J Cell Biol 220, e202012144.

Gell C, Bormuth V, Brouhard GJ, Cohen DN, Diez S, Friel CT, Helenius J, Nitzsche B, Petzold H, Ribbe J, *et al.* (2010). Microtubule dynamics reconstituted in vitro and imaged by single–molecule fluorescence microscopy. Methods Cell Biol 95, 221–245.

Gross P, Kumar KV, Goehring NW, Bois JS, Hoege C, Jülicher F, Grill SW (2019). Guiding self–organized pattern formation in cell polarity establishment. Nat Phys 15, 293–300.

Hahn I, Voelzmann A, Parkin J, Fülle JB, Slater PG, Lowery LA, Sanchez–Soriano N, Prokop A (2021). Tau, XMAP215/Msps and Eb1 co–operate interdependently to regulate microtubule polymerisation and bundle formation in axons. PLoS Genet 17, e1009647.

Han C, Jan LY, Jan YN (2011). Enhancer–driven membrane markers for analysis of nonautonomous mechanisms reveal neuron–glia interactions in Drosophila. Proc Natl Acad Sci USA 108, 9673–9678.

Heppert JK, Dickinson DJ, Pani AM, Higgins CD, Steward A, Ahringer J, Kuhn JR, Goldstein B (2016). Comparative assessment of fluorescent proteins for in vivo imaging in an animal model system. Mol Biol Cell 27, 3385–3394.

Howard J (2014). Quantitative cell biology: the essential role of theory. Mol Biol Cell 25, 3438–3440.

Joglekar AP, Bouck DC, Molk JN, Bloom KS, Salmon ED (2006). Molecular architecture of a kinetochore–microtubule attachment site. Nat Cell Biol 8, 581–585.

Kuo Y, Howard J (2021). In vitro reconstitution of microtubule dynamics and severing imaged by label–free interference reflection microscopy. ArXiv Prepr ArXiv210701501.

Kuo Y–W, Trottier O, Mahamdeh M, Howard J (2019). Spastin is a dual–function enzyme that severs microtubules and promotes their regrowth to increase the number and mass of microtubules. Proc Natl Acad Sci USA 116, 5533–5541.

Lawrimore J, Bloom KS, Salmon ED (2011). Point centromeres contain more than a single centromere–specific Cse4 (CENP–A) nucleosome. J Cell Biol 195, 573–582.

Leake MC, Chandler JH, Wadhams GH, Bai F, Berry RM, Armitage JP (2006). Stoichiometry and turnover in single, functioning membrane protein complexes. Nature 443, 355–358.

Liao M, Liang X, Howard J (2021). The narrowing of dendrite branches across nodes follows a well–defined scaling law. Proc Natl Acad Sci USA 118, e2022395118.

Magde D, Elson E, Webb WW (1972). Thermodynamic fluctuations in a reacting system measurement by fluorescence correlation spectroscopy. Phys Rev Lett 29, 705.

Martin–Fernandez ML, Tynan CJ, Webb SED (2013). A "pocket guide" to total internal reflection fluorescence. J Microsc 252, 16–22.

Mashanov GI, Tacon D, Peckham M, Molloy JE (2004). The spatial and temporal dynamics of pleckstrin homology domain binding at the plasma membrane measured by imaging single molecules in live mouse myoblasts. J Biol Chem 279, 15274–15280.

Matov A, Applegate K, Kumar P, Thoma C, Krek W, Danuser G, Wittmann T (2010). Analysis of microtubule dynamic instability using a plus–end growth marker. Nat Methods 7, 761–768.

Maurer SP, Bieling P, Cope J, Hoenger A, Surrey T (2011). GTPgammaS microtubules mimic the growing microtubule end structure recognized by end–binding proteins (EBs). Proc Natl Acad Sci USA 108, 3988–3993.

Maurer SP, Cade NI, Bohner G, Gustafsson N, Boutant E, Surrey T (2014). EB1 accelerates two conformational transitions important for microtubule maturation and dynamics. Curr Biol 24, 372–384.

Ori–McKenney KM, Jan LY, Jan YN (2012). Golgi outposts shape dendrite morphology by functioning as sites of acentrosomal microtubule nucleation in neurons. Neuron 76, 921–930.

Poe AR, Tang L, Wang B, Li Y, Sapar ML, Han C (2017). Dendritic space–filling requires a neuronal type–specific extracellular permissive signal in Drosophila. Proc Natl Acad Sci USA 114, E8062–E8071.

Pollard TD (2014). The value of mechanistic biophysical information for systems–level understanding of complex biological processes such as cytokinesis. Biophys J 107, 2499–2507.

Rolls MM, Satoh D, Clyne PJ, Henner AL, Uemura T, Doe CQ (2007). Polarity and intracellular compartmentalization of Drosophila neurons. Neural Dev 2, 1–15.

Roostalu J, Thomas C, Cade NI, Kunzelmann S, Taylor IA, Surrey T (2020). The speed of GTP hydrolysis determines GTP cap size and controls microtubule stability. eLife 9, e51992.

Rusan NM, Fagerstrom CJ, Yvon A–MMC, Wadsworth P (2001). Cell cycle–dependent changes in microtubule dynamics in living cells expressing green fluorescent protein–α tubulin. Mol Biol Cell 12, 971–980.

Seetapun D, Castle BT, McIntyre AJ, Tran PT, Odde DJ (2012). Estimating the microtubule GTP cap size in vivo. Curr Biol 22, 1681–1687.
Sen I, Veprintsev D, Akhmanova A, Steinmetz MO (2013). End binding proteins are obligatory dimers. PLoS One 8, 74448.
Stewart A, Tsubouchi A, Rolls MM, Tracey WD, Sherwood NT (2012). Katanin p60–like1 promotes microtubule growth and terminal dendrite stability in the larval class IV sensory neurons of Drosophila. J Neurosci 32, 11631–11642.
Stone MC, Roegiers F, Rolls MM (2008). Microtubules have opposite orientation in axons and dendrites of Drosophila neurons. Mol Biol Cell 19, 4122–4129.
Strothman C, Farmer V, Arpa G, Rodgers N, Podolski M, Norris S, Ohi R, Zanic M (2019). Microtubule minus–end stability is dictated by the tubulin off–rate. J Cell Biol 218, 2841–2853.
Taniguchi Y, Choi PJ, Li GW, Chen H, Babu M, Hearn J, Emili A, Sunney Xie X (2010). Quantifying E. coli proteome and transcriptome with single–molecule sensitivity in single cells. Science 329, 533–538.
Thevathasan JV, Kahnwald M, Cieśliński K, Hoess P, Peneti SK, Reitberger M, Heid D, Kasuba KC, Hoerner SJ, Li Y, *et al.* (2019). Nuclear pores as versatile reference standards for quantitative superresolution microscopy. Nat Methods 16, 1045–1053.
Tutucci E, Livingston NM, Singer RH, Wu B (2018). Imaging mRNA in vivo, from birth to death. Annu Rev Biophys 47, 85–106.
Ulbrich MH, Isacoff EY (2007). Subunit counting in membrane–bound proteins. Nat Methods 4, 319–321.
Uyemura T, Takagi H, Yanagida T, Sako Y (2005). Single–molecule analysis of epidermal growth factor signaling that leads to ultrasensitive calcium response. Biophys J 88, 3720–3730.
Wachsmuth M, Conrad C, Bulkescher J, Koch B, Mahen R, Isokane M, Pepperkok R, Ellenberg J (2015). High–throughput fluorescence correlation spectroscopy enables analysis of proteome dynamics in living cells. Nat Biotechnol 33, 384–389.
Wilson T (1990). Confocal Microscopy, London: Academic Press.
Wu J–Q, Pollard TD (2005). Counting cytokinesis proteins globally and locally in fission yeast. Science 310, 310–314.
Zanic M, Stear JH, Hyman AA, Howard J (2009). EB1 recognizes the nucleotide state of tubulin in the microtubule lattice. PLoS One 4, e7585.